

# Dalton Transactions

An international journal of inorganic chemistry

Accepted Manuscript

This article can be cited before page numbers have been issued, to do this please use: L. Santa maria de la parra, L. E. Riafrecha, G. A. Echeverría, L. Lezama, O. E. Piro, D. M. Gil, A. Frontera and I. Leon, *Dalton Trans.*, 2025, DOI: 10.1039/D5DT01463H.



This is an Accepted Manuscript, which has been through the Royal Society of Chemistry peer review process and has been accepted for publication.

Accepted Manuscripts are published online shortly after acceptance, before technical editing, formatting and proof reading. Using this free service, authors can make their results available to the community, in citable form, before we publish the edited article. We will replace this Accepted Manuscript with the edited and formatted Advance Article as soon as it is available.

You can find more information about Accepted Manuscripts in the [Information for Authors](#).

Please note that technical editing may introduce minor changes to the text and/or graphics, which may alter content. The journal's standard [Terms & Conditions](#) and the [Ethical guidelines](#) still apply. In no event shall the Royal Society of Chemistry be held responsible for any errors or omissions in this Accepted Manuscript or any consequences arising from the use of any information it contains.

## ARTICLE

## Structural, Spectroscopic, Theoretical, and Magnetic Investigations of a Novel Cubane-like Tetranuclear Copper(II)-Hydrazone Complex

Received 00th January 20xx,  
Accepted 00th January 20xx

DOI: 10.1039/x0xx00000x

Lucía Santa María de la Parra,<sup>a</sup> Leonardo E. Riafrecha,<sup>b</sup> Gustavo A. Echeverría,<sup>c</sup> Luis Lezama,<sup>d</sup> Oscar E. Piro,<sup>c</sup> Diego M. Gil,<sup>e</sup> Antonio Frontera<sup>f</sup> and Ignacio E. León\*<sup>a,g</sup>

This study details the synthesis of a novel ligand, (E)-5-chloro-N'-(2-hydroxy-3-methoxybenzylidene) thiophene-2-carbohydrazide ligand (for short, H<sub>2</sub>L), and its tetranuclear Cu(II) complex (Cu<sub>4</sub>L<sub>4</sub>), together with their X-ray crystal structures and the magnetic properties and EPR spectra of Cu<sub>4</sub>L<sub>4</sub> within 4–300 K temperature range. Furthermore, we report the spectroscopic characterization (FTIR and UV-Vis) of the compounds and perform a Hirshfeld analysis of their non-covalent interactions, along with certain quantum chemical calculations. H<sub>2</sub>L crystallizes in the monoclinic space group Cc with Z = 8 molecules per unit cell, and Cu<sub>4</sub>L<sub>4</sub> complex in the tetragonal space group P4<sub>1</sub>/a with Z = 4. The complex is at a crystal site of S<sub>4</sub> symmetry, conforming to a cubane-like Cu<sub>4</sub>O<sub>4</sub> core. The main path for exchange interaction between neighboring copper ions in the core involves a relatively large overlap of copper d(x<sup>2</sup>-y<sup>2</sup>) electron ground state orbital with the sp<sup>2</sup> lone-pair lobes of the bridging oxygen. Magnetic susceptibility in the 5–300 K range, mainly interpreted with the exchange Hamiltonian  $\hat{H}_{ex} = -J(\hat{S}_1 \cdot \hat{S}_2 + \hat{S}_1 \cdot \hat{S}_3 + \hat{S}_1 \cdot \hat{S}_4 + \hat{S}_2 \cdot \hat{S}_3 + \hat{S}_2 \cdot \hat{S}_4 + \hat{S}_3 \cdot \hat{S}_4)$ , confirms the expected relatively strong antiferromagnetic (AF) character of the complex ( $J = -61.5(1) \text{ cm}^{-1}$ ). The powder room temperature Q-band EPR spectrum shows a very broad band ( $\Delta B_{pp} = 1980$  Gauss) corresponding to a gyromagnetic g-factor of 2.13. The band intensity decreases sharply with temperature, as expected for a Cu(II) tetramer with a well isolated spin singlet ( $S = 0$ ) ground state.

## Introduction

Copper coordination compounds exhibit a broad spectrum of chemical-biological activities, making them valuable in catalysis, electrochemistry, medicinal chemistry and diagnostic applications, among other areas.(1–4)

The nuclearity of copper complexes, namely the number of metal ions in the cluster, influences their properties, including reactivity, stability and their potential applications in catalysis or materials science.(5)

Copper can form complexes with different nuclearities, depending on the coordination environment and the oxidation state of the metal. These complexes can be classified into various categories based on the nuclearity: mononuclear, binuclear, trinuclear, tetranuclear, hexanuclear Cu(II) clusters, as well as coordination polymers.(6)

Particularly, the nature and chemistry of polynuclear Cu(II) complexes have brought the interest of several research groups for their unconventional structure, but also for potential applications in the different disciplines like catalysis, inorganic biochemistry, bioinorganic chemistry, electronic and magnetism.(7–10) Because they can function as both chelating and bridging agents at the same time, multidentate Schiff bases are frequently utilized to create polynuclear copper complexes.(11,12) Their diverse interactions arise from the redox properties of copper ion and the structural versatility of their ligands.

In this order, hydrazones are a class of organic compounds that feature the functional group  $\text{C}=\text{NNH}_2$ . They are formed by the condensation of a carbonyl compound (such as an aldehyde or ketone) with hydrazine ( $\text{NH}_2\text{--NH}_2$ ) or a hydrazine derivative. This family of ligands has several applications related to its antibacterial, anticancer, and antituberculosis activity.(13–15)

Several reports describe different copper-hydrazones complexes with diverse nuclearities (mononuclear, binuclear, tetranuclear) and geometries exhibiting catalytic, anticancer and magnetic properties.(6,16–19)

<sup>a</sup> CEQUINOR (UNLP, CCT-CONICET La Plata, asociado a CIC), Departamento de Química, Facultad de Ciencias Exactas, Universidad Nacional de La Plata. Blvd. 120 N° 1465, 1900 La Plata, Argentina.

<sup>b</sup> CEDECOR (UNLP-CICBA), CONICET, Departamento de Química, Facultad de Ciencias Exactas, Universidad Nacional de La Plata, 47 y 115, 1900 La Plata, Argentina

<sup>c</sup> Departamento de Física, Facultad de Ciencias Exactas, Universidad Nacional de La Plata and Institute IFLP (CONICET, CCT-La Plata), C.C. 67, 1900 La Plata, Argentina.

<sup>d</sup> Department of Inorganic Chemistry, University of the Basque Country (UPV/EHU), Sarriena 48940, Leioa, Spain.

<sup>e</sup> INBIOFAL (CONICET – UNT). Instituto de Química Orgánica. Facultad de Bioquímica, Química y Farmacia. Universidad Nacional de Tucumán. Ayacucho 471. T4000CAN. San Miguel de Tucumán. Argentina.

<sup>f</sup> Departament de Química, Universitat de les Illes Balears, Crta de Valldemossa km 7.5, 07122 Palma de Mallorca, Spain.

<sup>g</sup> Cátedra de Fisiopatología, Departamento de Ciencias Biológicas, Facultad de Ciencias Exactas, Universidad Nacional de La Plata. 47 y 115, La Plata 1900, Argentina.

\*Corresponding author: ileon@biol.unlp.edu.ar.

Supplementary Information available: [details of any supplementary information available should be included here]. See DOI: 10.1039/x0xx00000x

ARTICLE

Journal Name

Copper(II) complexes, particularly those containing cubane-like  $\text{Cu}_4\text{O}_4$  cores, have been extensively researched to design magnetic materials. (20,21)

A classification of cubane-like complexes based on the distribution of Cu-O distance values inside the cube has been proposed by Mergehenn and Haase. (22–24) Compounds that exhibit dominant AF interactions and four long Cu-O distances between two pseudo dimeric units are classified as type I, whereas compounds that exhibit dominant ferromagnetic interactions and two long distances within each pseudo dimeric unit are classified as type II. Alternatively, Ruiz and coworkers (25) categorized cubane compounds according to Cu...Cu distances as follows: (i) [2 +4], complexes with two short and four long Cu...Cu distances; (ii) [4 +2], complexes with four short and two long Cu...Cu distances; and (iii) [6 +0], complexes with six equivalent Cu...Cu distances.

The original aim of our research is the synthesis, structure, physicochemical and spectroscopic properties of hydrazones with potential chemical-biological activity and their complexes with transition metals, in a search for improved pharmaceutical performance.

As it turns out, the Cu(II) complex with the new  $\text{H}_2\text{L}$  ligand crystallizes as a tetranuclear, cubane-like cluster,  $\text{Cu}_4\text{L}_4$ , with unique structural features: (i) It is located at a crystallographic site of symmetry  $S_4$  of the tetragonal space group  $I4_1/a$  that renders equivalent the four metals ions; (ii) Neighbouring metals are bridged by a single hydroxyl oxygen atom along the metal electron  $d(x^2-y^2)$  ground state orbital and through the oxygen  $sp^2$  lone-pair lobes that closely fulfils the Anderson-Goodenough-Kanamori rules for strong AF coupling; (iii) The bulky  $\text{Cu}_4\text{L}_4$  complex is electrically neutral and as a molecular crystal lacks of counterions and solvent molecules. Furthermore, the X-ray structure shows no significant intermolecular H-bonding. All these make the tetranuclear units relatively isolated from one another in the lattice.

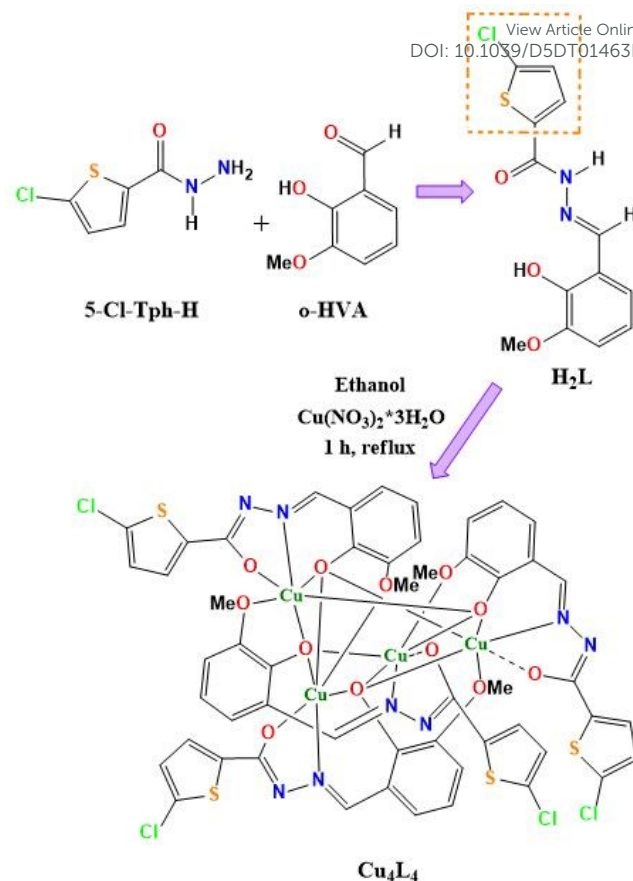
All the above fortunate characteristics make the  $\text{Cu}_4\text{L}_4$  crystal an ideal system for magnetic-structural studies to shed further light on the super-exchange interaction between the unpaired electrons on neighbouring copper ions in a cluster. A subject of considerable interest, as exchange coupling plays a fundamental role in the nature of the chemical bond and in the magnetic properties of a wide range of materials

We report here the synthesis of a new ligand ( $\text{H}_2\text{L}$ ) and its tetranuclear Cu(II) complex ( $\text{Cu}_4\text{L}_4$ ), their X-ray crystal structures and the magnetic properties and EPR spectra in the 4-300K temperature range of  $\text{Cu}_4\text{L}_4$ . Also, we present the spectroscopic characterization of the compounds, a Hirshfeld analysis of their non-covalent bonding and some quantum chemical calculations.

## Results and discussion

### Synthetic procedure

The synthesis of ligand ( $\text{H}_2\text{L}$ ) and complex ( $\text{Cu}_4\text{L}_4$ ) was carried out following previously published methods with certain modifications. (26–29) Scheme 1 summarized the synthesis of the ligand and the complex (see details in experimental section).



**Scheme 1.** Synthesis of the ligand and complex  $\text{Cu}_4\text{L}_4$ .

### Nuclear magnetic resonance

The solid-state X-ray structure of the  $\text{H}_2\text{L}$  ligand was validated in solution by 1D and 2D NMR spectra (Figures SI1–SI3).  $^1\text{H}$  and  $^{13}\text{C}$  spectra were obtained in  $d^6$ -DMSO solvent on a Bruker Advance NEO 500 MHz equipment.

$^1\text{H}$  NMR spectra showed peak of OH at 12.13 and 11.92, the characteristic peak of amide H at 10.59(9.36) ppm, while the imine peak was observed at 8.65(8.49) ppm. This peak confirms the binding between the hydrazide and aldehyde group. Additionally, the methyl fragment of ligand was observed at 3.84(3.82) ppm.  $^{13}\text{C}$  NMR showed the signal of the ketone group of amide fragments at 160.40(156.95) ppm. 2D spectra (Figure SI3) confirm the above assignment of peaks. The explanation for the signals of NMR study are that the NH1 nitrogen experiences a very slowly enantiomeric equilibrium or the presence in solution of the keto-enol equilibrium, that were reported by other authors as El-Gammal and coworkers for similar metal complexes (30).

### Crystallography

Crystal data and structure refinement results for  $\text{H}_2\text{L}$  and  $\text{Cu}_4\text{L}_4$  are summarized in the supplementary Table X1.

**$\text{H}_2\text{L}$  ligand:** An ORTEP (31) drawing of the electrically neutral  $\text{H}_2\text{L}$  ligand is shown in Fig. 1. There are two very closely related

molecules per asymmetric unit (*rms* separation between homologous atoms from their best least-square fit of 0.031 Å).

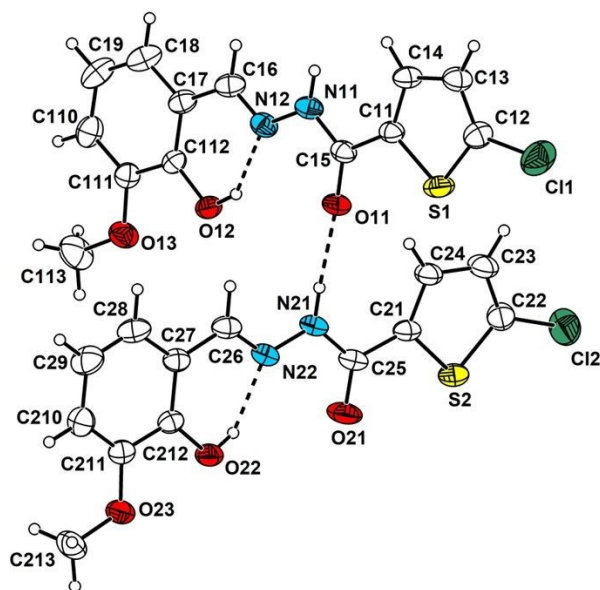


**Figure 1.** View of  $H_2L$ , showing the labelling of the non-H atoms and their displacement ellipsoids at the 30% probability level. Intra and intermolecular H-bonds are indicated by dashed lines.

Bond distances within one of the two independent  $H_2L$  molecules are compared in Table X2 with the corresponding ones of its  $L^{2-}$  ligand anion in the  $Cu_4L_4$  complex.

Because of extended bond delocalization, both ligand molecules are nearly planar (*rms* deviation of non-H atoms from the best least-squares plane less than 0.07 Å); they are angled with each other in 69.17(3)°. Planarity is further favoured by an intra-molecular OH...N bond [O...N bond distances of 2.600(4) and 2.590(4) Å and corresponding O-H...N bond angles of 144 and 143°].

Observed bond distances and angles conform established Organic Chemist knowledge. Particularly, benzene C-C bond distances in the 1.370(7)-1.411(5) Å range for molecule #1 and 1.364(6)-1.412(5) Å for #2 agree with a ring resonant-bond structure. Halo-substituted thiophene ring C-C bond lengths of 1.363(5), 1.403(5) and 1.339(5) Å for #1 and 1.355(5), 1.403(6) and 1.333(5) Å for #2 accords with an expected alternate double-single-double bond structure. Single bond C-S distances are 1.712(4) and 1.704(4) Å for #1 and 1.717(4) and 1.699(4) for #2. C(th)-Cl bond lengths are 1.722(4) and 1.718(4) Å. Within the  $-(C_6H)=Ni_2-(Ni_1H)-(C_5=O_i)-$  ( $i = 1, 2$ ) molecular fragments, the short imine  $C_6-Ni_2$  lengths of 1.268(5) and 1.269(5) Å contrast with the longer amide  $C_5-Ni_1$  distances of 1.348(5) and 1.355(5) Å values, clearly confirming the formally double and single bond characters for these links. Neighbouring independent molecules are linked to each other through a  $NH...O=C$  bond [ $d(N...O) = 2.944(4)$  Å,  $\angle (N-H...O) = 161^\circ$ ]. The crystal is further stabilized by a complex intermolecular H-bond network of weak  $NH...O$ ,  $CH...O$ , and  $CH...Cl$  interactions. The H-bonding structure is detailed in the supplement Table X7a.

**$Cu_4L_4$  complex:** The  $CuL$  units are arranged in the lattice as a tetranuclear  $Cu_4L_4$  complex located at a special crystallographic position of  $S_4 = \bar{4}$  site symmetry. Fig. 2 shows the crystal asymmetric unit content of the complex, and corresponding Cu-ligand bond distances and angles are in Table X3.

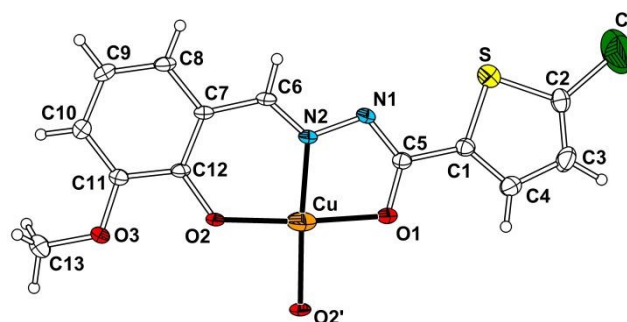


**Figure 2.** Crystal asymmetric unit ( $CuL$ ) of tetranuclear  $Cu_4L_4$  complex showing the labelling of the non-H atoms and their displacement ellipsoids at the 30% probability level. Copper-ligand bonds are indicated by solid lines. The tetragonal crystal  $c$ -axis is along the vertical. For convenience, the distorted square coordination around  $Cu(II)$  ions has been completed with the hydroxyl oxygen atom  $O2'$  of a neighbouring, symmetry-related,  $CuL$  unit of the same tetranuclear complex ( $S_4$  site symmetry operation:  $-\frac{1}{4} + y, \frac{1}{4} - x, \frac{1}{4} - z$ ).

Copper ion is in a distorted square environment,  $CuO_3N$  core, coordinated by a nearly planar  $L^{2-}$  molecule acting as a tridentate ligand through its deprotonated hydroxyl oxygen atom [ $d(Cu-O_2) = 1.957(2)$  Å], carbonyl oxygen [ $d(Cu-O_1) = 1.934(2)$  Å] and the imine N-atom [ $d(Cu-N_2) = 1.918(2)$  Å], nearly along their  $sp^2$  electron lone-pair lobes. The fourth ligand (at the square basis) is the deprotonated hydroxyl oxygen atom  $O2'$  [ $d(Cu-O_2') = 1.980(2)$  Å] of a neighbouring, symmetry-related,  $CuL$  unit (see Fig. 2), which coordinates the metal along the other oxygen  $sp^2$  electron lone-pair lobe. *Cis* L-Cu-L bond angles are in the 82.0(1)-94.63(9)° range and *trans* L-Cu-L bond angles are 173.68(9) and 175.2(1)°. The observed square coordination around  $Cu(II)$  ion indicates a  $d(x^2-y^2)$  electron (or hole) ground state.

Besides a 180°-rotation of the thiophene ring around the linking  $>C-C(thio)<$   $\sigma$ -bond, upon hydroxyl and amine deprotonation of neutral ligand molecule and binding to copper, the major structural changes of  $L^{2-}$  ligand occur, as expected, at the bonding involving the chelating-to-copper atoms (see Table X2). In fact, the formal  $-(C=O)-(NH)-N=(CH)-$  bond structure of  $H_2L$  shows C=O, (CO)-(NH), (NH)-N, and N=(CH) bond lengths of 1.223(4), 1.348(5), 1.379(4) and 1.268(5) Å, respectively. It transforms into the formal  $-(C-O)=N-N=(CH)-$  bond structure of  $L^{2-}$  ligand, with observed C-O, (CO)-N-, N--N, and N=(CH) bond distances of 1.286(4), 1.307(4), 1.391(3) and 1.275(4) Å, respectively. The  $>C(ph)-OH$  bond length of  $H_2L$  does not change significantly in the corresponding  $>C(ph)-O-$  link of  $L^{2-}$  ligand [from 1.350(4) to 1.352(3) Å].

By application to the  $CuL$  unit of Fig. 2 the rotation-reflection operations of crystallographic  $S_4$  site symmetry (in the tetragonal



space group  $I4_1/a$ ) it is obtained the tetranuclear  $\text{Cu}_4\text{L}_4$  complex shown in Fig. 3.

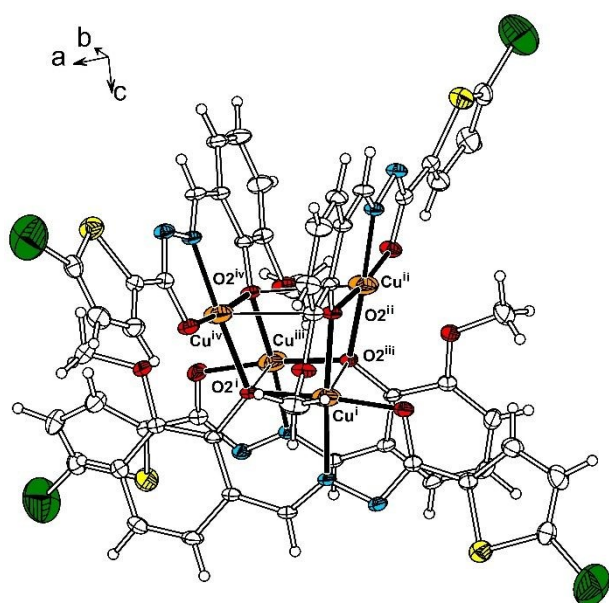


**Figure 3.** View of  $\text{Cu}_4\text{L}_4$  complex. For clarity, only the symmetry-related copper and bridging hydroxyl oxygen atoms are labelled. Stronger coordination bonds are in full lines and weaker Cu-ligand contacts in thin lines. Chlorine, sulphur, oxygen, and nitrogen atoms are respectively indicated in green, yellow, red and blue coloured ellipsoids.  $S_4$  site-symmetry operations (i)  $x, y, z$ ; (ii)  $-1/4+y, 1/4-x, 1/4-z$ ; (iii)  $-x, 1/2-y, z$ ; (iv)  $1/4-y, 1/4+x, 1/4-z$ .

#### Vibrational spectroscopy

We compared the FTIR vibrational absorption spectra for the solid samples of complex and ligand recorded in the 4000–400  $\text{cm}^{-1}$  frequency range (Fig. SI4, Table X10). The absence in the spectrum of the complex of IR bands assigned to the OH and NH groups in the ligand spectrum correlates with the tridentate coordination of the ligand through its donor atoms O, N, and O as revealed by structural X-ray diffraction. Besides, the effect of the coordination of Cu(II) by the oxygen atom of the carboxyl group could be appreciated by the red shift of the 1639  $\text{cm}^{-1}$  band in the spectrum of the ligand to 1617  $\text{cm}^{-1}$  in the complex. Furthermore, we attribute the weak bands at 484  $\text{cm}^{-1}$  and 444  $\text{cm}^{-1}$  in the spectrum of the complex, which are absent in the ligand spectrum, to Cu–N and Cu–O stretching modes, respectively. Similar spectroscopic results were described by us for other copper thiophen hydrazones complexes.(26–29)

#### Electronic spectroscopy

The UV-vis electronic absorption spectra of the ligand and its Cu(II) complex were recorded in dimethyl sulfoxide (DMSO) solutions. As can be seen in Fig. SI5, bands with very different molar absorptivity were selectively registered using varying concentrations in DMSO solutions of the complex. The spectrum of the complex exhibits a broad band with a maximum at 696 nm, which is typical of a copper  $d-d$  transitions, as we previously observed for similar compounds. (17,26,29) We assigned this band with the lowest energy to  $d(xy) \rightarrow d(x^2-y^2)$  and  $d(z^2) \rightarrow d(x^2-y^2)$  electronic transitions, consistent with the distorted square planar geometry around the

copper ion observed in the crystal structure. The more energetic transitions  $d(yz) \rightarrow d(x^2-y^2)$  and  $d(xz) \rightarrow d(x^2-y^2)$  overlaps with the more intense band with maximum at 409 nm corresponding to ligand-to-metal charge transfer transitions (LMCT), thus giving rise to a shoulder at 431 nm. Intra-ligand transitions were assigned to the band at 340 nm with a shoulder at 354 nm since the free ligand's spectra (Fig. SI4) displays an absorption maximum at 322 nm with a shoulder at 344 nm. These findings correlate with the solid-state spectrum, with the variations in the maxima being attributed to the various techniques employed in their acquisition. Since these differences are minimal, it can be inferred that there are no significant changes in the coordination environment of Cu from the solid to the solution. The described assignments of both the solid and DMSO solution of complex are listed on Table 1.

**Table 1.** Experimental electronic spectra of the complex in DMSO solution and in the solid state. Band maxima are given in nm. The molar absorptivity (in  $\text{M}^{-1}\text{cm}^{-1}$ ) is in parentheses. The proposed assignment is also given.

| EXPERIMENTAL IN DMSO<br>( $\epsilon$ , $\text{M}^{-1}\text{cm}^{-1}$ ) | EXPERIMENTAL, SOLID SAMPLE | ASSIGNMENT        |
|--|----------------------------|-------------------|
| 696 (80)   | 721                        | $d \rightarrow d$ |
| 431 (shoulder)   | 411 (shoulder)             | $d \rightarrow d$ |
| 409 ( $1.6 \times 10^4$ )  | 387                        | LMCT              |
| 354 (shoulder)   | 341                        | Intra-ligand      |

contacts, represented as spikes labelled 1 in the FP plots comprise 21.9 and 20.8% for molecules 1 and 2, respectively.

#### Theoretical calculations

The theoretical study focuses on analyzing the Cu–O interactions within the tetranuclear core of compound  $\text{Cu}_4\text{L}_4$ , as depicted in Fig. 4a. Notably, some Cu–O contacts, with distances as long as 2.707 Å, are better described as noncovalent regium bonds (RgBs) rather than conventional coordination or semi-coordination bonds, which typically exhibit stronger covalent character.

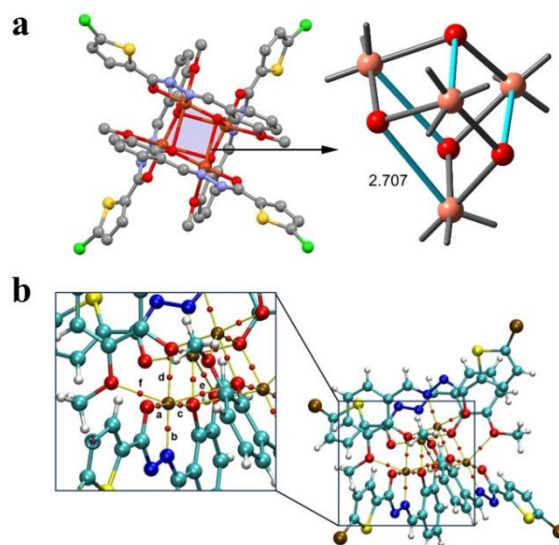


**Figure 4.** (a) Partial view of compound Cu<sub>4</sub>L<sub>4</sub> with an amplification of the Cu<sub>4</sub>O<sub>4</sub> central core (distance in Å). The four symmetrically equivalent long distances are represented in blue. (b) QTAIM distribution of bond critical points (red spheres) and bond paths (yellow lines) interconnecting the Cu atoms which are involved in coordination and regium bonds.

Regium bonding refers to a class of noncovalent interactions in which an electrophilic site on a group 11 metal (Rg = Cu, Ag, Au) interacts attractively with a nucleophilic region either intramolecularly or intermolecularly. The strength and geometry of these interactions are influenced by the electronic nature of the metal center, the nucleophilic donor, and the substituent effects on the surrounding molecular framework. Recent studies (32) have shown that even remote substituents (e.g., para-substituted pyridines) can modulate the strength of Cu...Nu regium bonds in supramolecular systems. Remarkably, RgBs have also been shown (33) to drive the formation of unusual anion...anion networks, as observed for CuCl<sub>4</sub><sup>2-</sup> and CuBr<sub>4</sub><sup>2-</sup> dianions, where short Cu...Cl/Br contacts enable copper centers to behave as electrophiles within an overall negatively charged environment. These findings underscore the versatility of regium bonding and its ability to organize both neutral and charged building blocks into well-defined architectures. They also highlight the broader importance of  $\pi$ -hole interactions in directing the supramolecular behavior of group 11 elements.

To investigate the presence of a  $\pi$ -hole (a region of positive potential perpendicular to a molecular framework) in compound Cu<sub>4</sub>L<sub>4</sub>, a mononuclear model complex was utilized, namely CuL(H<sub>2</sub>O), where a water molecule was added to complete one of the coordination positions. In the tetranuclear system of compound Cu<sub>4</sub>L<sub>4</sub>,  $\pi$ -holes are not apparent as they are already engaged with the oxygen atoms of neighbouring molecules. The inclusion of water serves a dual purpose: firstly, to complete the square-planar environment of the copper ion, and secondly, to establish a neutral model for analysis. The molecular electrostatic potential (MEP) surface of CuL(H<sub>2</sub>O) is depicted in Fig. SI9. It can be noted that the MEP maximum occurs at the hydrogen atoms of the coordinated water molecule, which is considered irrelevant as this water molecule is only included in the theoretical model but is not present in the solid-state structure of Cu<sub>4</sub>L<sub>4</sub>. The MEP values are significantly negative at the oxygen and nitrogen atoms of the ligand, with values ranging from -31.4 kcal/mol at the nitrogen atom to -37.0 kcal/mol at the oxygen atom of the methoxy group. Notably, the MEP is positive at the copper atom, confirming the presence of two  $\pi$ -holes above and below the molecular plane, with a MEP value of +21.9 kcal/mol, which highlights its electrophilic nature.

The QTAIM analysis conducted on the tetranuclear system aims to distinguish between regium Cu...O bonds and classical Cu-O coordination bonds. As illustrated in Fig. 4b, each Cu-N,O bond features a bond critical point (BCP, marked as a red sphere) and a bond path (indicated by an orange line) linking the Cu atom to the O or N atoms. Each Cu atom is connected to two O atoms and one N atom from the same ligand, as well as to three O-atoms from adjacent ligands. These BCPs are labelled "a-f" in Fig. 4b, with their parameters detailed in Table 2.

**Table 2.** Topological parameters in a.u. at the bond critical points connecting the Cu(II) ion to the O or N-atoms.

| BCP <sup>a</sup> | $\rho(r)$ | $\nabla^2\rho(r)$ | $V(r)$      | $G(r)$ | $H(r)$      | $\lambda_2$ | Distance<br>Cu-X (X =<br>N, O) | Type   |
|------------------|-----------|-------------------|-------------|--------|-------------|-------------|--------------------------------|--------|
| A                | 0.0928    | 0.4329            | -<br>0.1630 | 0.1356 | -<br>0.0273 | -<br>0.1235 | 1.934<br>(Cu-O1)               | coord. |
| B                | 0.1091    | 0.4322            | -<br>0.1869 | 0.1475 | -<br>0.0394 | -<br>0.1471 | 1.917<br>(Cu-N2)               | coord. |
| C                | 0.0833    | 0.4230            | -<br>0.1479 | 0.1268 | -<br>0.0211 | -<br>0.1069 | 1.957<br>(Cu-O2)               | coord. |
| D                | 0.0794    | 0.3958            | -<br>0.1392 | 0.1191 | -<br>0.0201 | -<br>0.1049 | 1.980<br>(Cu-O2)               | coord. |
| E                | 0.0173    | 0.0629            | -<br>0.0141 | 0.0149 | 0.0008      | -<br>0.0137 | 2.707<br>(Cu...O3)             | RgB    |
| F                | 0.0358    | 0.1689            | -<br>0.0434 | 0.0428 | -<br>0.0006 | -<br>0.0406 | 2.327<br>(Cu...O2)             | RgB    |

<sup>a</sup> The labels of bond CPs are shown in Fig. 4b.

It is to be noted that the charge density at the BCPs labeled "a-d" exceeds 0.075 a.u., and the values of  $|V|$  (absolute value of potential energy density) are greater than  $G$  (kinetic energy density), indicative of typical coordination bonds.(34) These four BCPs are part of the bond paths defining the square-planar coordination around the Cu atom. Conversely, the other two BCPs, labelled "e" and "f", are associated with  $\rho$  values less than 0.04 a.u. and  $|V|$  approximately equal to  $G$ , characteristics of noncovalent interactions. Specifically, for the longer Cu...O distance at BCP labelled "e", the total energy density ( $H$ ) is positive, and the  $\rho$  value is notably small (0.0173 a.u.), suggesting weak noncovalent interactions. This QTAIM analysis indicates that the formation of the tetranuclear cluster in compound Cu<sub>4</sub>L<sub>4</sub> is not solely governed by coordination bonds but also involves two regium bonding interactions that significantly influence the final structure of the compound.

To substantiate the noncovalent nature of the interactions further, we analysed the two-dimensional maps of the Laplacian of the electron density ( $\nabla^2\rho$ ) overlaid with the reduced density gradient (RDG) 2D map. These combined maps are instrumental in distinguishing between coordination bonds, which generally involve covalency, and regium bonds, which are predominantly noncovalent. This analysis is depicted in Fig. 5, using a 2D plane defined by the Cu, O2', and O3'' atoms involved in the regium bonds. This plane also includes the N2 and O2 atoms forming coordination bonds, as detailed in Table 2, along with the short Cu-O, N distances (< 2.0 Å).

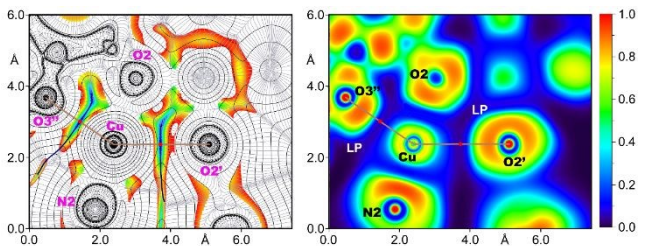


**Figure 5.** Left: 2D plot of the Laplacian (dashed lines for negative values and solid lines for positive ones) including the gradient lines (in grey) overlapped with the 2D RDG map for compound  $\text{Cu}_4\text{L}_4$ . Right: ELF 2D map of compound  $\text{Cu}_4\text{L}_4$  represented in the plane defined by the Cu, O2', and O3''. The bond paths are represented as brown lines and BCPs as red dots. The RDG density cut-off is 0.05 a.u. symmetry operations: ' -x, 1/2-y, z; '' -1/4+y, 1/4-x, 1/4-z.

The 2D  $\nabla^2\rho$  analysis shows positive values (marked by solid line iso-contours) between the O and Cu atoms, covering both coordination and regium bonds. This is coupled with the 2D-RDG maps, which display blue iso-contours specifically in the regions between Cu and the O2', O3'' atoms, effectively differentiating the coordination bonds (Cu–N2 and Cu–O2) from the regium bonds (RgBs) involving Cu...O2' and Cu...O3'' atoms (symmetry operations: ' -x, 1/2-y, z; '' -1/4+y, 1/4-x, 1/4-z). The BCPs and bond paths indicative of RgBs are highlighted on the 2D maps in Fig. 5, aligned with the zero flux boundaries between Cu and O atoms where RDG values are near zero.

The electron localization function (ELF) 2D map further delineates the distinct nature of Cu...O, N coordination and regium bonds. It shows maximum ELF values at the lone pairs of the N, O-donor atoms (in red) and highlights the electrophilic character of the Cu atom. Additionally, the ELF map reveals that the regions between the O2 and N2 atoms and the Cu atom, connected by coordination bonds, are blue (ELF  $\approx$  0.2), indicating some degree of electron localization (electron sharing). In contrast, RgBs are marked by BCPs (red dots) located in areas of minimal electron density (black color), typical of noncovalent interactions. The negative values of the second eigenvalue of the Hessian matrix ( $\lambda_2$ ) across all cases, as listed in Table 2, confirm that both coordination bonds and RgBs are attractive forces.

## Magnetic properties

### Copper bonding structure

The copper and hydroxyl oxygen (O2) atoms are located at the vertices of a distorted cube, conforming to a cubane-like  $\text{Cu}_4\text{O}_4$  core tetramer. This is compared in Fig. 6 with a schematic ideal cubane  $\text{Cu}_4\text{O}_4$  core.

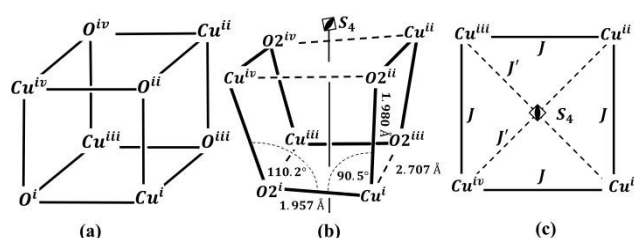


**Figure 6.** (a) Ideal cubane  $\text{Cu}_4\text{O}_4$  core ( $T_d$  symmetry). (b) Cubane-like  $\text{Cu}_4\text{O}_4$  core in tetranuclear  $\text{Cu}_4\text{L}_4$  complex (crystallographic site symmetry  $S_4$ , a subgroup of  $T_d$ ) showing super-exchange relevant Cu-O bond paths (in full lines) distances (Å) and Cu-O-Cu bond angles (°). Some weaker Cu...O paths are indicated by thin lines. Symmetry operations as in Fig. 3. (c) Exchange coupling scheme used in the spin Hamiltonian of eqn (2).

The actual case of the  $\text{Cu}_4\text{O}_4$  core tetramer in  $\text{Cu}_4\text{L}_4$  complex corresponds to a reduction of the ideal point symmetry  $T_d$  to its subgroup  $S_4$ , where every one of all four Cu(II) ions are equally linked to other two neighbouring metals through hydroxyl oxygen bridges, -Cu-O2-Cu' (Cu-O2 = 1.957(2) Å; O2-Cu' = 1.980(2) Å), nearly along the oxygen  $sp^2$  electron lone-pair orbitals (Cu-O2-Cu' bond angle of 110.2(1)°) in such a way to nearly optimize the overlap with the Cu(II) magnetic  $d(x^2-y^2)$  orbitals (O2-Cu-O2' bond angle of 90.50(9)°). As established by Anderson-Goodenough-Kanamori rules (35–37), this binding structure (see schematic Fig. SI10), favours a relatively large AF super-exchange coupling between the unpaired electrons of neighbouring Cu(II) ions.(35–38)

### Magnetic susceptibility

Magnetic susceptibility data for polycrystalline samples of  $\text{Cu}_4\text{L}_4$  were collected between 5 and 300 K in an applied field of 0.1 T. The temperature dependence of the molar magnetic susceptibility  $\chi$  and the  $\chi T$  product are displayed in Fig. 7. Both plots show the usual characteristics of molecular systems with predominantly AF couplings and a well isolated  $S = 0$  ground state.

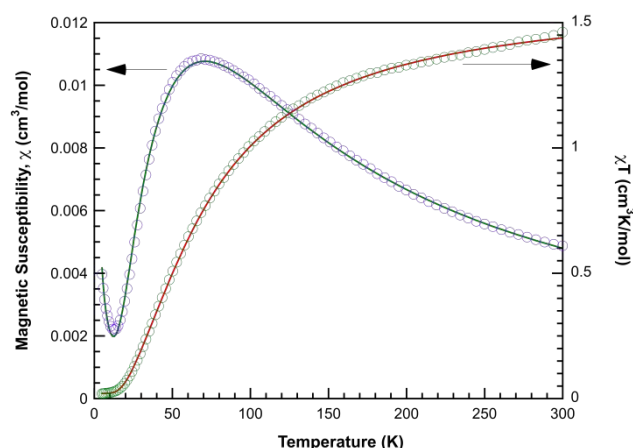


**Figure 7.** Magnetic behaviour of compound  $\text{Cu}_4\text{L}_4$ . The solid lines represent the best least-squares fit to experimental data of eqn (4) with  $J = -61.5(1) \text{ cm}^{-1}$ ,  $J' = 1(1) \text{ cm}^{-1}$  and  $\rho = 0.0013$ .

The  $\chi T$  value at 300 K (1.45  $\text{cm}^3\text{K}/\text{mol}$ ) is slightly smaller than expected for four uncoupled Cu(II) ions with a positive orbital contribution to the magnetic effective moment ( $\chi T = 1.70 \text{ cm}^3\text{K}/\text{mol}$  with  $g = 2.13$  from EPR results). Upon cooling, the  $\chi T$  product continuously decreases and almost stabilizes at a value of 0.02  $\text{cm}^3\text{K}/\text{mol}$  below 10 K. Magnetic susceptibility increases continuously with decreasing temperature, reaching a broad maximum at around 68 K. Below this temperature, the curve drops to a minimum at 13 K and then rises sharply upon further cooling. The increase of susceptibility at low temperatures and the residual moment of 0.02  $\text{cm}^3\text{K}/\text{mol}$  could be attributed to a small amount of paramagnetic impurity. On the other hand, the thermal variation of  $\chi^{-1}$  appears to follow the Curie-Weiss law  $\chi_C^{-1} = (T - \theta)/C_m$  above 150 K with  $C_m = 1.75 \text{ cm}^3\text{K}/\text{mol}$  ( $g = 2.16$ ) and  $\theta = -63.2 \text{ K}$  (Fig. SI11 of SI). However, the value of  $C_m$  is slightly larger than expected and is probably overestimated due to the presence of strong AF interaction.



The observed magnetic behaviour has been analysed through the isotropic Heisenberg-Dirac-van Vleck model Hamiltonian to describe the energy of the low-lying electronic spin states:

$$\hat{H}_{ex} = -\sum_{i<j} J_{ij} \hat{S}_i \cdot \hat{S}_j \tag{1}$$

where  $J_{ij}$  is the exchange integral between the magnetic centres  $i$  and  $j$  and corresponds to the spin-dependent pair-wise electrostatic electron-electron interaction arising from the Pauli's exclusion principle.(39,40) Bearing in mind the  $S_4$  point symmetry of the  $Cu_4O_4$  core tetramer in  $Cu_4L_4$ , a distorted [4+2] geometric type of cubane according to the model proposed by Ruiz *et al.*(25) two different intramolecular exchange pathways can be operative in this compound: (a) that involving two short Cu-O bonds: Cu-O2 = 1.957(2) Å; O2-Cu' = 1.980(2) Å; Cu...Cu' = 3.2283(6) Å, (b) the one involving one short and one long Cu-O distances: Cu-O2 = 1.957(2) Å; O2-Cu'' = 2.707(2) Å; Cu...Cu' = 3.6275(8) Å (Fig. 6). Therefore, assuming that all spin multiplets are well isolated and hence the total spin  $S$ , is a good quantum number, the resulting spin Hamiltonian is:

$$\hat{H} = g\beta B \hat{S} - J(\hat{S}_1 \cdot \hat{S}_2 + \hat{S}_2 \cdot \hat{S}_3 + \hat{S}_3 \cdot \hat{S}_4 + \hat{S}_4 \cdot \hat{S}_1) - J'(\hat{S}_1 \cdot \hat{S}_3 + \hat{S}_2 \cdot \hat{S}_4) \tag{2}$$

where the Arabic numbering of the spins follows the roman ones of the copper atoms in Fig. 6,  $J$  and  $J'$  are the coupling parameters through the (a) and (b) pathways, respectively,  $\beta$  is the Bohr magneton,  $B$  is the applied magnetic field vector, and  $g$  is the average Lande factor for the coupled system, where the individual  $g$ -factors of all Cu(II) ions are equal because the crystallographic  $S_4$  site symmetry.

Considering the energies of the spin states resulting from eqn (2), the following analytical expression for the thermal dependence of the magnetic susceptibility per mol of tetramer could be derived (see Section M2 of SI):

$$\chi_m(T) = \frac{0.7503 \frac{g^2}{N} \times}{1 + 6 \exp(y) + [\exp(y-x)]^2 + 3 \exp(2y-x) + 5 \exp(2y+x)} \tag{3}$$

where  $x = J/kT$ ,  $y = J'/kT$ ,  $N$  and  $k$  are the Avogadro and Boltzmann constants, respectively. Considering the residual moment observed at low temperatures, eqn (3) has been extended to include a paramagnetic contribution, assumed to come from a species with the same molecular weight per Cu(II) ion and  $g$ -value as the main compound to avoid overparameterization:

$$\chi_{calc}(T) = (1 - \rho)\chi_m + \rho \frac{0.375 \frac{g^2}{T}}{T} \tag{4}$$

Least-squares fitting of the experimental data with eqn (4) leads to  $J = -59.8(3) \text{ cm}^{-1}$  (AF),  $J' = +15(3) \text{ cm}^{-1}$ ,  $g = 2.107(3)$  and  $\rho = 0.0013(1)$ . The calculated  $\chi_{calc}$  vs  $T$  and  $\chi_{calc}T$  vs  $T$  curves reproduce well the experimental data and the agreement factors, defined as  $R_\chi = \sum(\chi_{obs} - \chi_{calc})^2 / \sum \chi_{obs}^2$  and  $R_{\chi T} = \sum(\chi T_{obs} - \chi T_{calc})^2 / \sum (\chi T_{obs})^2$ , are  $9.9e^{-5}$  and  $4.6e^{-5}$ , respectively, which corresponds to a good experiment vs theory agreement. The sign and magnitude of  $J$  agree well with what is expected from the disposition of the magnetic orbitals involved in the exchange pathway (a) and is stronger than those reported in the literature for other related compounds (see Table 3). As

mentioned above, an effective overlap between the  $d(x^2-y^2)$  orbitals of the Cu(II) ion, where mainly the unpaired electrons are located, is achieved via the oxygen  $sp^2$  electron lone-pair orbitals (Fig. SI10). It is to be noted that general observations show that tetranuclear Cu(II) complexes with Cu-O-Cu bridges that satisfy Anderson-Goodenough-Kanamori rules often feature AF coupling between neighbouring copper ions, irrespective of cluster symmetry.(40)

**Table 3.** Comparison of exchange interaction in  $Cu_4L_4$  with other published cubane-like tetranuclear Cu(II) complexes having exact or approximated  $S_4$  symmetry

| Reference                                | $J \text{ (CM}^{-1}\text{)}$ | $J' \text{ (CM}^{-1}\text{)}$ |
|--|------------------------------|-------------------------------|
| Bencini <i>et al.</i> (1987) (41)        | -12.2                        | +0.6                          |
| Manna <i>et al.</i> (2017) (8)           | -20.3                        | +0                            |
| Papadakis <i>et al.</i> (2013) (7)       | -21.7                        | +7.6                          |
| Koningsbruggen <i>et al.</i> (1993) (42) | No significant interaction   | No significant interaction    |
| This work                                | -61.5(3)                     | +1(1)                         |

As far as the value of  $J'$  is concerned, its positive sign is not surprising, since it has already been proposed from theoretical calculations (43) and has been observed experimentally (7) in compounds with exchange paths like (b), but its magnitude is significantly larger than expected. It should be noted that the presence of a paramagnetic impurity does not have a significant effect on the determination of the  $J$  value, but it does affect the  $J'$  value due to its strong influence on the low temperature magnetic susceptibility values. In fact, an undesirable correlation between the values of  $g$ ,  $J'$  and  $\rho$  has been observed in the least squares fit. The same problem arises when the energies of the spin states are obtained from a full-matrix diagonalization of the Hamiltonian in eqn (2) using the PHI software package.(44) In this case, the best fit is obtained with  $J = -58.4 \text{ cm}^{-1}$ ,  $J' = 22 \text{ cm}^{-1}$ ,  $g = 2.097$  and  $\rho = 0.0019$ , being  $R_\chi = 2.6e^{-4}$  and  $R_{\chi T} = 3.0e^{-5}$ . Finally, to reduce the correlation between the variables, it was decided to remove  $g$  as a variable to be optimized and to set its value to 2.13, obtained from the Q-band EPR measurements. With this constraint, the best fit is obtained with of  $J = -61.5(1)$ ,  $J' = 1(1)$  and  $\rho = 0.0013$  ( $R_\chi = 2.6e^{-4}$ ,  $R_{\chi T} = 7.5e^{-5}$ ), and the calculated curves are shown as solid lines in Fig. 7.

The zero-field spin relative energies ( $E$ ) are derived from eqn (9) in Section M1 of SI and their ordering for the exchange parameters obtained from the above analysis of the temperature dependence of magnetic susceptibility is shown in Fig. 8.



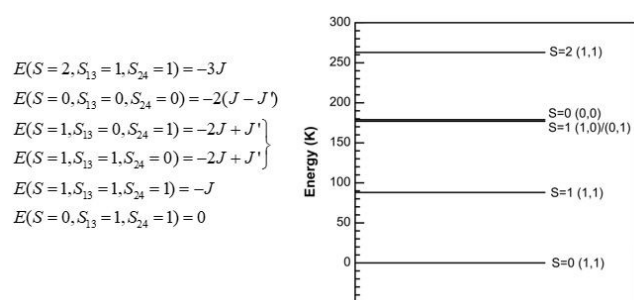


**Figure 8.** Spin zero-field energy levels of  $\text{Cu}_4\text{L}_4$  for the best least-squares fitting exchange parameters  $J = -61.5(1)$  and  $J' = 1(1) \text{ cm}^{-1}$  obtained through magnetic susceptibility measurements in the 5–300 K temperature range.

The first excited triplet is 88 K above the ground singlet, while the two degenerate triplets are at 177.3 K and the quintet even higher at 263.8 K. Therefore, all triplets of the  $\text{Cu}_4$  cluster are largely depopulated at low temperatures, confirming that the triplet EPR spectra observed below 20 K (see below) must originate from a binuclear impurity. The exchange interaction between the two  $\text{Cu(II)}$  ions of this compound must necessarily be very small, since its magnetic susceptibility can be satisfactorily fitted with Curie's law. On the other hand, the anomalous Curie constant obtained from the analysis of the inverse of the magnetic susceptibility at high temperatures is explained by the large value obtained for the main exchange interaction within the tetramer. Strict Curie-Weiss behaviour below room temperature should not be expected, given the relatively large  $J = -61.5 \text{ cm}^{-1}$  value (see Sect. M3 of SI).

### EPR spectra

The X-band EPR signal of polycrystalline powder samples of  $\text{Cu}_4\text{L}_4$  (Fig. SI12a of SI) is barely detectable at room temperature, but the Q-band spectrum clearly shows a very broad nearly isotropic signal ( $\Delta B_{\text{pp}} = 1980 \text{ Gauss}$ ) which can be satisfactorily fitted with a Lorentzian line profile giving a value of  $g = 2.13$  (Fig. SI12b). The intensity of this signal decreases rapidly with temperature, while its linewidth decreases only slightly. This behaviour is in good agreement with that expected for a  $\text{Cu(II)}$  tetramer with strong AF interactions. The large linewidth is mainly due to the presence of several spin states with the same  $S$  value, which facilitates fast relaxation via isotropic exchange.<sup>(45)</sup> In addition, at room temperature the superposition of transitions from different EPR active spin states (three triplets and one quintuplet) with different zero-field splitting is expected, which may contribute to line broadening.

On the other hand, a narrow but very weak signal centred around  $g = 2.10$  is also detected in the spectra recorded at room temperature. The intensity of this signal increases continuously, and its linewidth decreases with decreasing temperature (Fig. 9a), taking the expected shape for an axially symmetric  $g$ -tensor which is common in  $\text{Cu(II)}$  systems whose ground state is  $d(x^2-y^2)$ .<sup>(46)</sup> A hyperfine structure is clearly observed in the low-field region of the spectrum (Fig. 9a) at temperatures below 20 K. The large number of peaks observed in the parallel component of the spectrum and the relatively low separation between them rule out

the possibility that this signal originates from a monomeric species. We shall consider this EPR signature as due to transitions within the triplet ( $S=1$ ) state of a weakly coupled ( $J < 4 \text{ K}$ ) binuclear  $\text{Cu(II)}$  impurity in the  $\text{Cu}_4\text{L}_4$  lattice. This is like the case of the binuclear impurity found by Bencini *et al.* (1986) at 4.2 K in the lattice of the strong AF ( $J = -107 \text{ K}$ ) binuclear complex  $[(\text{dien})\text{Cu}(\text{ox})\text{Cu}(\text{tmen})(\text{H}_2\text{O})_2](\text{ClO}_4)_2$  (dien = diethylenetriamine; ox = oxalato; tmen = N,N,N',N'-tetramethylethylenediamine).<sup>(41)</sup> spectrum was analysed with the following spin Hamiltonian:

$$\hat{H} = \beta \mathbf{B} \cdot \mathbf{g} \cdot \hat{\mathbf{S}} + \hat{\mathbf{S}} \cdot \mathbf{D} \cdot \hat{\mathbf{S}} + \hat{\mathbf{S}} \cdot \mathbf{A} \cdot (\hat{\mathbf{I}}_1 + \hat{\mathbf{I}}_2) = \beta \mathbf{B} \cdot \mathbf{g} \cdot \hat{\mathbf{S}} + D \left( \hat{S}_z^2 - \frac{2}{3} \right) + E \left( \hat{S}_x^2 - \hat{S}_y^2 \right) + \hat{\mathbf{S}} \cdot \mathbf{A} \cdot \hat{\mathbf{I}}_1 + \hat{\mathbf{S}} \cdot \mathbf{A} \cdot \hat{\mathbf{I}}_2, \quad (5)$$

where  $g$ ,  $D$ , and  $A$  are respectively the gyromagnetic, fine and hyperfine tensors,  $\hat{\mathbf{S}}$  the total electron spin  $\hat{\mathbf{S}} = \hat{\mathbf{S}}_1 + \hat{\mathbf{S}}_2$  with  $S_1 = S_2 = \frac{1}{2}$  and  $S = 1$  and nuclear spins  $I_1 = I_2 = \frac{3}{2}$  are uncoupled to each other. The spectrum can be satisfactorily adjusted with the following parameters:  $g_{\parallel} = 2.304$ ;  $g_{\perp} = 2.027$ ;  $D = 0.0107 \text{ cm}^{-1}$ ;  $E = 0.0024 \text{ cm}^{-1}$ ;  $A_{\parallel} = 0.0078 \text{ cm}^{-1}$ ;  $A_{\perp} < 0.0030 \text{ cm}^{-1}$  (Fig. 9b). It is noteworthy that the calculated value of  $A_{\parallel}$  is about half of the expected value for a  $\text{Cu(II)}$  ion in a square-based pyramidal environment. This suggests that the hyperfine splitting corresponds to the interaction of unpaired electrons with two copper nuclei and not with four, as would be expected from the tetrameric structure of the compound.

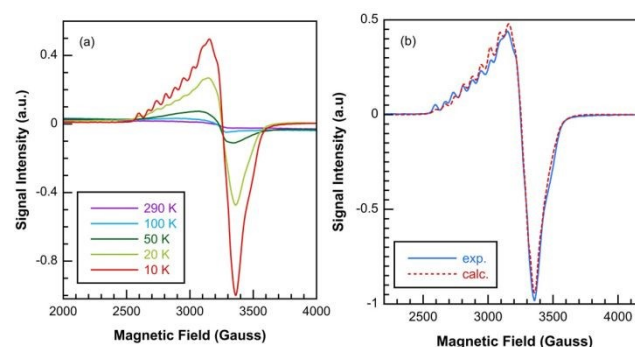


**Figure 9.** (a) Thermal evolution of the X-band EPR spectrum of a  $\text{Cu}_4\text{L}_4$  powder sample. (b) Experimental and theoretical EPR spectrum at 4 K.

To determine whether this triplet spectrum is indeed due to one of the  $S = 1$  states of the  $\text{Cu}_4$  cluster, single crystal EPR studies were carried out. In the Q-band spectrum recorded at room temperature, the tetramer signal could be detected, confirming that its large linewidth is less due to the possible superposition of transitions in different states than to the existence of very efficient relaxation mechanisms (Fig. SI13). However, in the X-band spectra, which were performed on different single crystals and orientations, no signal could be detected for any temperature in the range of 4 to 300 K. Therefore, it appears that a binuclear impurity, either from the synthesis process or from the crushing of the crystals, is responsible for the triplet spectrum observed at low temperatures in the spectra recorded from polycrystalline samples. However, given the limited number and size of single crystals that could be analysed, it cannot be ruled out that the

spectrum is due to defects in the structure of some of the tetramers, e.g. copper vacancies.

## Experimental section

### Synthesis

The synthesis of ligand and complex were performed following procedures reported previously with modifications.(26–29,47)

#### (E)-5-chloro-N'-(2-hydroxy-3-methoxy-benzylidene)thiophene-2-carbohydrazide (H<sub>2</sub>L)

Briefly, the ligand was obtained from the condensation reaction of 5-Chlorothiophene-2-carboxylic acid hydrazide (5-Cl-Tph-H) and 3-methoxysalicyl aldehyde (o-vanillin, o-HVA) presented in Scheme 1. Ethanolic solution of o-HVA (0.152 g, 1 mmol) was added dropwise on ethanolic solution of 5-Cl-Tph-H (0.177 g, 1 mmol) and then stirred in reflux for 1 h. The solvent was allowed to slowly evaporate at room temperature for a month before light-yellow needle-shaped crystals were produced, filtered and washed with cold ethanol. (Yield: 98%)

<sup>1</sup>H NMR (500 MHz, DMSO-*d*<sub>6</sub>) δ 12.13 (s, 1H, OH), 11.92 (s, 1H, OH'), 10.59 (s, 1H, NH(or OH)), 9.36 (s, 1H, NH'), 8.65 (s, 1H, H-4), 8.49 (s, 1H, H-4'), 7.88 (d, *J* = 4.2 Hz, 1H, H-2), 7.80 (d, *J* = 4.1 Hz, 1H, H-2'), 7.46 (d, *J* = 7.9 Hz, 1H, H-3), 7.27 (dd, *J* = 6.7, 4.0 Hz, 2H, H-3', ArH), 7.19 (d, *J* = 7.9 Hz, 1H, ArH'), 7.04 (dd, *J* = 8.2, 4.1 Hz, 2H, ArH, ArH'), 6.92 (t, *J* = 8.0 Hz, 1H, ArH), 6.87 (t, *J* = 7.9 Hz, 1H, ArH'), 3.84 (s, 3H, CH<sub>3</sub>O), 3.82 (s, 3H, CH'<sub>3</sub>O).

<sup>13</sup>C NMR (126 MHz, DMSO-*d*<sub>6</sub>) δ 160.40(C-1), 156.95(C-1'), 148.62 (ArC, ArC'), 148.44 (ArC, ArC'), 148.19(C-6), 147.47(C-5), 146.74(C-5'), 141.79(C-6'), 137.69(C-2), 134.69 (C-3), 131.12(C-2'), 129.58(C-3'), 128.86(C-4), 126.92(C-4'), 121.12 (ArC), 120.69 (ArC'), 119.94 (ArC), 119.59 (ArC'), 117.82 (ArC, ArC'), 114.30 (ArC), 113.57(ArC'), 56.37(CH<sub>3</sub>O), 56.31(C'H<sub>3</sub>O).

#### Cu<sub>4</sub>L<sub>4</sub>

Following with the same synthesis procedure of ligand, an ethanolic solution of copper (II) nitrate trihydrate (g, mmol) was added dropwise on ethanolic solution of N-N-Cl-Tph (g, mmol) and then stirred in reflux for 1 h. Dark green needle-shaped crystals were obtained after 6 weeks of slow evaporation of the solvent at room temperature. These were filtered and washed with cold ethanol. (Yield: 79%)

### Spectroscopy

Infrared spectra of solid samples (KBr pellets) were recorded with a Bruker Equinox 55 instrument (Billerica, MA, United States) in the 4000–400 cm<sup>-1</sup> region. Raman spectra were measured with a WITEC alpha 300 RA spectrophotometer, using a laser excitation wavelength of 532 nm and a 20x objective lens.

Electronic spectra of the complex and ligand were measured using a Shimadzu UV-2006 spectrophotometer. UV-Vis spectra were recorded in a solution of dimethyl sulfoxide (DMSO) using 10 mm quartz cells in the spectral range from 250 to 800 nm. The diffuse reflectance spectrum of solid samples was recorded using a BaSO<sub>4</sub> pellet as a reference with an integrating sphere attachment, in the 250–800 nm range, and it was forward-converted to absorbance using the Kubelka–Munk function.(48)

### X ray diffraction data

View Article Online

DOI: 10.1039/D5DT01463H

The measurements were performed on an Rigaku-Oxford, Gemini, Eos CCD diffractometer with graphite-monochromate MoK $\alpha$  ( $\lambda$  = 0.71073 Å) radiation. X-ray diffraction intensities were collected ( $\omega$  scans with  $\theta$  and  $\kappa$ -offsets), integrated and scaled with CrysAlisPro suite of programs.(49) The unit cell parameters were obtained by least-squares refinement (based on the angular setting for all collected reflections with intensities larger than seven times the standard deviation of measurement errors) using CrysAlisPro. Data were corrected empirically for absorption employing the multi-scan method implemented in CrysAlisPro. The structures were solved by intrinsic phasing with SHELXT (50) and the molecular models refined by full-matrix least-squares procedure with SHELXL.(51)

**H<sub>2</sub>L (ligand):** There are two molecules per asymmetric unit. Most H-atoms were found in a difference Fourier map phased on the heavier atoms. However, they were positioned geometrically and refined with the riding model. The methyl H-atoms were treated as rigid groups allowed to rotate during the refinement around the corresponding O-CH<sub>3</sub> bonds, such as to maximize the sum of the residual electron density at the hydrogen calculated positions. The -CH<sub>3</sub> group converged to a staggered rotational conformation. The hydroxyl H-atoms were refined by a similar procedure by which the O-H groups are allowed to rotate around the corresponding C(ph)-OH bonds such as to maximize the residual electron density at the hydrogen calculated positions. The molecule absolute structure was determined through anomalous dispersion, mainly from the chlorine and sulphur atoms.

**[Cu<sub>4</sub>L<sub>4</sub>] (complex):** All H-atoms were found at approximate positions in a difference Fourier map phased on the heavier atoms. However, they were positioned at their expected geometrical locations and refined with the riding model. The methyl H-atoms were refined as described for H<sub>2</sub>L.

### Hirshfeld surfaces calculations

Hirshfeld surfaces and their associated two-dimensional fingerprint plots (full and decomposed) (52–56) have been generated using the CrystalExplorer21.5 program (57) to visualize and quantify the main intermolecular interactions which are responsible for the crystal packing of both compounds. The Hirshfeld surfaces were mapped over  $d_{\text{norm}}$ , shape index and curvedness properties. The  $d_{\text{norm}}$  (normalized contact distance) surface was computed by using two distances  $d_e$  (the distance from the point to the nearest nucleus external to the surface),  $d_i$  (the distance of the nearest nucleus internal to the surface) and the van der Waals (vdW) radii of the atoms involved in the intermolecular interaction. The  $d_{\text{norm}}$  surfaces were mapped over a fixed colour scale of -0.025 a.u. (red) to 0.55 a.u. (blue) and -0.05 a.u. (red) to 0.75 a.u. (blue) for H<sub>2</sub>L and Cu<sub>4</sub>L<sub>4</sub>, respectively. Graphical representations of  $d_{\text{norm}}$  Hirshfeld surfaces show a colour code of red (shorter contacts), white (contacts with a distance equal to the sum of van der Waals radii of atoms), and blue (longer contacts). The Hirshfeld surfaces mapped over shape index and curvedness properties are especially useful to identify planar  $\pi$ -stacking interactions.(52) The two-dimensional fingerprint (FP)

## ARTICLE

## Journal Name

plots were displayed using the expanded 0.6–2.8 Å range, and reciprocal contacts were also included.

### Theoretical Methods

The geometries of the complexes included in this study were computed at the PBE0-D3/def2-TZVP level of theory (58–60) using the crystallographic coordinates within the Gaussian-16 program. (61) The “atoms-in-molecules” (AIM)(62) analysis of the electron density has been performed at the same level of theory using the Multiwfn program. (63) The electron density vs electrostatic potential plots, reduced density gradient (RDG) 2D plots, (64) and ELF 2D plots (65) were computed using Multiwfn program. (63) The QTAIM analysis was represented using the VMD software. (66) The Laplacian of electron density can be decomposed into the sum of contributions along the three principal axes of maximal variation, giving the three eigenvalues of the Hessian matrix ( $\lambda_1$ ,  $\lambda_2$ , and  $\lambda_3$ ). The sign of  $\lambda_2$  can be utilized to distinguish bonding (attractive,  $\lambda_2 < 0$ ) weak interactions from non-bonding ones (repulsive,  $\lambda_2 > 0$ ). (64)

### Magnetic data

Temperature dependent magnetic susceptibility measurements were performed between 5 and 300 K with an applied field of 0.1 T, using an MPMS3 SQUID magnetometer (Quantum Design). The experimental susceptibilities were corrected for the diamagnetism of the constituent atoms, by using Pascal tables, and the sample holder.

X-band EPR measurements were carried out on a Bruker ELEXSYS 500 spectrometer equipped with a super-high-Q resonator ER-4123-SHQ and a maximum available microwave power of 200 mW. Powder samples were placed in quartz tubes and spectra were recorded at different temperatures between 4 and 300 K using standard Oxford Instruments low temperature devices. A single crystal of about 0.25 x 0.31 x 0.81 mm<sup>3</sup> was glued to a cleaved KCl cubic holder with its larger edge parallel to an edge of the KCl crystal. The sample holder was glued to an L-shaped quartz rod and rotated with respect to the applied magnetic field using a manual Bruker goniometer. EPR spectra were recorded at different temperatures rotating the crystal around the X, Y and Z axes. The magnetic field was calibrated with an NMR probe and the frequency inside the cavity (~ 9.4 GHz) was determined with an integrated MW-frequency counter. For Q-band studies, EPR spectra on powder and single crystals were recorded at room temperature on a Bruker EMX system equipped with an ER-510-QT resonator. The frequency inside the cavity (~34 GHz) was determined with a Hewlett-Packard 5352B microwave frequency counter. Data were collected and processed using the Bruker Xepir suite.

### Conclusions

In summary, we report here the synthesis and X-ray crystal structure of a new ligand, (E)-5-chloro-N'-(2-hydroxy-3-methoxybenzylidene) thiophene-2-carbohydrazide (H<sub>2</sub>L) and its tetranuclear Cu(II) complex, Cu<sub>4</sub>L<sub>4</sub>. The complex crystallizes in the tetragonal space group *P*4<sub>1</sub>/*a* at a special position of *S*<sub>4</sub> symmetry that renders equivalent all metals and oxygen atoms of the

cubane-like Cu<sub>4</sub>O<sub>4</sub> core. The theoretical identification of  $\pi$ -hole features at the Cu centers, confirmed through electrostatic potential mapping and QTAIM/NCI analyses, correlates well with the experimentally observed short Cu...O contacts in the crystal structures. These geometrical parameters, which deviate from typical coordination geometries, suggest the operation of noncovalent attractive interactions consistent with  $\pi$ -hole-driven regium bonding. Thus, the computational insights not only support the classification of these interactions as RgBs but also help explain the directional supramolecular assembly observed in the solid state. Neighbouring copper ions are bridged at short bond distances by hydroxyl oxygen atoms (Cu–O distances of about 1.97 Å) along the metal  $d(x^2-y^2)$  ground state orbitals and through the oxygen  $sp^2$  electron lone-pair lobes (bridging Cu–O–Cu angle of 110.2°). This bonding structure closely complies with the Anderson-Goodenough-Kanamori rules for strong AF exchange coupling between unpaired electrons in the Cu(II) cluster, as revealed from magnetic susceptibility measurements in the 5–300 K temperature range. These experiments can be interpreted mainly in terms of the highly symmetric spin Hamiltonian of eqn (2) that provides the exchange-coupled spin energy levels, followed by van Vleck's quantum statistics treatment of magnetic properties. The best least-squares fitting of van Vleck's analytical magnetic susceptibility to the experimental data leads to a relatively strong AF exchange coupling constant  $J = -61.5 \text{ cm}^{-1}$ . This gives rise to a spin singlet ( $S = 0$ ) energy ground state, a triplet ( $S = 1$ ) at 88 K above the ground singlet, two degenerate triplets along a singlet at 177 K and a quintet ( $S = 2$ ) at 264 K. Moreover, spectroscopy studies including FTIR and UV-Vis afforded a complete characterization of the new complex.

As expected, the high temperature susceptibility closely follows the Curie-Weiss behaviour of an AF molecular magnet. In fact, a least-squares fitting of Curie-Weiss law to experimental data for  $T > 150 \text{ K}$  leads to a  $\vartheta$ -value of -63.2 K. We also show (SI) that in the limit of high temperatures ( $|J|/kT \ll 1$ ) the expansion of the analytical susceptibility to first order in  $|J|/kT$  reduces to an AF Curie-Weiss behaviour where  $\vartheta$  is a linear function of the exchange coupling constant  $J$ .

The room temperature Q-band EPR spectrum of powdered Cu<sub>4</sub>L<sub>4</sub> complex (SI) shows a nearly isotropic ( $g$ -factor of 2.13) and very broad band ( $\Delta B_{pp} = 1980 \text{ Gauss}$ ). This large bandwidth is the result of several contributions, including fast relaxation through isotropic exchange promoted by the presence of several spin states with the same  $S$  value and the superposition of transitions from different EPR active spin states (three triplets and one quintuplet) with different zero-field splitting. The band intensity diminishes sharply with temperature due to thermal depopulation of the EPR-active excited states of the strong Cu<sub>4</sub>L<sub>4</sub> antiferromagnet.

Besides, a narrow and very weak signal centred around  $g = 2.10$  is also detected in the room temperature EPR spectra. The X-band EPR intensity of this signal increases continuously, and its linewidth sharpens with decreasing temperature, hence indicating the presence of paramagnetic impurity with an axially symmetric  $g$ -tensor associated with a  $d(x^2-y^2)$  electron ground state. The rich hyperfine structure observed in the low-field region of the spectrum at low temperature indicates a Cu(II) binuclear species. The spectrum was interpreted with the spin Hamiltonian of eqn (5)

which satisfactorily accounted for the spectral features with the best least-squares fitting parameters  $g_{||} = 2.304$ ,  $g_{\perp} = 2.027$ ;  $D = 0.0107 \text{ cm}^{-1}$ ,  $E = 0.0024 \text{ cm}^{-1}$ ;  $A_{||} = 0.0078 \text{ cm}^{-1}$ ,  $A_{\perp} < 0.0030 \text{ cm}^{-1}$ .

## Author contributions

Conceptualization: L.S.M.D.L.P, I.E.L. Data curation: L.S.M.D.L.P, L.E.R, O.E.P, G.A.E., D.M.G, L.L. Funding acquisition: O.E.P, G.A.E, D.M.G, A.F, I.E.L. Investigation: L.S.M.D.L.P, I.E.L. Methodology: L.S.M.D.L.P, D.M.G Supervision: L.L, A.F, I.E.L. Writing – original draft: L.S.M.D.L.P, L.E.R, O.E.P, G.A.E, D.M.G, L.L, I.E.L. Writing – review & editing: O.E.P, L.L, D.M.G, A.F, I.E.L.

## Conflicts of interest

There are no conflicts to declare.

## Data availability

The data supporting this article have been included as part of the Supplementary Information:

**X-ray crystallographic data.** Tables of crystal data for  $\text{H}_2\text{L}$  ligand and its  $\text{Cu}_4\text{L}_4$  complex (Table X1), bond distances of  $\text{H}_2\text{L}$  and charged  $\text{L}_2^-$  ligand in  $\text{Cu}_4\text{L}_4$  complex (Table X2), bond lengths and angles around copper in  $\text{Cu}_4\text{L}_4$  complex (Table X3), fractional coordinates and equivalent isotropic displacement parameters of the non-H atoms of  $\text{H}_2\text{L}$  ligand and the  $\text{Cu}_4\text{L}_4$  complex (Tables X4a,b), full bond distances and angles (Tables X5a,b), atomic anisotropic displacement parameters (Tables X6a,b), hydrogen atoms positions (Tables X7a,b), torsion bond angles (Tables X8a,b), and H-bond distances and angles (Table X9a), assignment of the most significant vibrational modes for  $\text{H}_2\text{L}$  and  $\text{Cu}_4\text{L}_4$  (Table X10). Crystallographic structural data have been deposited at the Cambridge Crystallographic Data Centre (CCDC). Any request to the Cambridge Crystallographic Data Centre for this material should quote the full literature citation and the reference number CCDC 2260992 ( $\text{H}_2\text{L}$ ) and 2260081 ( $\text{Cu}_4\text{L}_4$ ).

**Magnetic properties.** Unpaired electrons spin levels and analytical expression for magnetic susceptibility (Sect. M1); Magnetic susceptibility (Sect. M2); Curie-Weiss behaviour (Sect. M3); Powder EPR spectra (Sect. M4), and Single crystal EPR spectra (Sect. M5).

## Acknowledgements

We thank CONICET (Grant PIP 0651, PIP 2051, PIP 215) ANPCyT (PICT-Serie A-02988, PICT 2019-2322) and UNLP (Grant 11/X857, EX005) of Argentina for financial support. D.M.G, G.A.E, I.E.L and O.E.P are Research Fellows of CONICET. This work has been supported by the Gobierno de España, MICIU/AEI (Project PID2020-115637GB-I00). D.M.G. thanks SCAIT-UNT (Project D728).

## References

1. Pu Y, Chen S, Yang Y, Mao X. Copper-based biological alloys and nanocomposites for enzymatic catalysis and sensing applications. *Nanoscale*. 2023;15(28):11801–12.
2. León IE. Transition metal complexes: a new generation of anticancer drugs. *Future Med Chem*. 2024 Sep 9;16(17):1727–30.
3. Liu W, Lin W, Yan L, Xu W, Yang J. Copper homeostasis and cuproptosis in cancer immunity and therapy. *Immunol Rev*. 2024 Jan 16;321(1):211–27.
4. Zhou M, Tian M, Li C. Copper-Based Nanomaterials for Cancer Imaging and Therapy. *Bioconjug Chem*. 2016 May 18;27(5):1188–99.
5. Nuricumbo-Escobar JJ, Campos-Alvarado C, Rocha-Alonso F, Ríos-Moreno G, Morales-Morales D, Höpfl H, et al. Versatile nuclearity in copper complexes with ortho functionalized 1,3-bis(aryl)triazenido ligands. *Inorganica Chim Acta*. 2010 Apr;363(6):1150–6.
6. Tripathi K, Drew MGB, Mathew G, Jaiswal-Nagar D, Calzado CJ, Mishra L. Crafting copper complexes of variable nuclearity and coordination geometry through solvent tailoring: Unveiling novel structure, magnetic insight and computational marvels. *J Mol Struct*. 2025 Feb;1321:139817.
7. Papadakis R, Rivière E, Giorgi M, Jamet H, Rousselot-Pailley P, Réglie M, et al. Structural and Magnetic Characterization of a Tetranuclear Copper(II) Cubane Stabilized by Intramolecular Metal Cation- $\pi$  Interactions. *Inorg Chem*. 2013 May 20;52(10):5824–30.
8. Manna SC, Manna S, Paul A, Zangrando E, Figuerola A, Dolai S, et al. Structural and Magnetic Characterization of Two Tetranuclear Cu(II) Complexes with Closed-Cubane-Like Core Framework. *ChemistrySelect*. 2017 Apr 13;2(11):3317–22.
9. López-Gastélum KA, Velázquez-Contreras EF, García JJ, Flores-Alamo M, Aguirre G, Chávez-Velasco D, et al. Mononuclear and Tetranuclear Copper(II) Complexes Bearing Amino Acid Schiff Base Ligands: Structural Characterization and Catalytic Applications. *Molecules*. 2021 Dec 1;26(23):7301.
10. Espindola-Moreno O, da Silva Moura F, Santa Maria de la Parra L, Stellet C, Serna JDP, Diniz R, et al. Antiproliferative activity of a series of copper(II) complexes derived from a furan-containing N-acylhydrazone: monomers, dimers, charge status, and cell mechanistic studies on triple negative breast cancer cells. *Dalton Transactions*. 2025;54(9):3872–86.



## ARTICLE

## Journal Name

11. Barwiolek M, Jankowska D, Kaczmarek-Kędziera A, Lakomska I, Kobylarczyk J, Podgajny R, et al. New Dinuclear Macrocyclic Copper(II) Complexes as Potentially Fluorescent and Magnetic Materials. *Int J Mol Sci.* 2023 Feb 3;24(3):3017.
12. Nunes P, Yildizhan Y, Adiguzel Z, Marques F, Costa Pessoa J, Acilan C, et al. Copper(II) and oxidovanadium(IV) complexes of chromone Schiff bases as potential anticancer agents. *JBIC Journal of Biological Inorganic Chemistry.* 2022 Feb 24;27(1):89–109.
13. Popiołek Ł. Updated Information on Antimicrobial Activity of Hydrazide–Hydrazones. *Int J Mol Sci.* 2021 Aug 30;22(17):9389.
14. Kumar P, Narasimhan B. Hydrazides/Hydrazones as Antimicrobial and Anticancer Agents in the New Millennium. *Mini-Reviews in Medicinal Chemistry.* 2013 Apr 1;13(7):971–87.
15. Mathew B, Suresh J, Ahsan M, Mathew G, Usman D, Subramanyan P, et al. Hydrazones as a Privileged Structural Linker in Antitubercular Agents: A Review. *Infect Disord Drug Targets.* 2015 Jul 29;15(2):76–88.
16. Patel AK, Jadeja RN, Roy H, Patel RN, Patel SK, Butcher RJ, et al. Copper(II) hydrazone complexes with different nuclearities and geometries: Synthesis, structural characterization, antioxidant SOD activity and antiproliferative properties. *Polyhedron.* 2020 Aug;186:114624.
17. Balsa LM, Ferraresi-Curotto V, Lavecchia MJ, Echeverría GA, Piro OE, García-Tojal J, et al. Anticancer activity of a new copper(II) complex with a hydrazone ligand. Structural and spectroscopic characterization, computational simulations and cell mechanistic studies on 2D and 3D breast cancer cell models. *Dalton Transactions.* 2021 Jul 28;50(28):9812–26.
18. Vrdoljak V, Pavlović G, Maltar-Strmečki N, Cindrić M. Copper(II) hydrazone complexes with different nuclearities and geometries: synthetic methods and ligand substituent effects. *New Journal of Chemistry.* 2016;40(11):9263–74.
19. Rodríguez MR, Balsa LM, Del Plá J, García-Tojal J, Pis-Diez R, Parajón-Costa BS, et al. Synthesis, characterization, DFT calculations and anticancer activity of a new oxidovanadium(IV) complex with a ligand derived from O-vanillin and thiophene. *New Journal of Chemistry.* 2019;43(29):11784–94.
20. Venegas-Yazigi D, Aravena D, Spodine E, Ruiz E, Alvarez S. Structural and electronic effects on the exchange interactions in dinuclear bis(phenoxo)-bridged copper(II) complexes. *Coord Chem Rev.* 2010 Sep;254(17–18):2086–95.
21. Turba S, Foxon SP, Beitat A, Heinemann FW, Petukhov K, Müller P, et al. Syntheses, Characterization, and Magnetic Studies of Copper(II) Complexes with the Ligand N,N,N',N'-Tetrakis(2-pyridylmethyl)-1,3-benzenediamine (1,3-tpbd) and its Phenol Derivative 2,6-Bis[bis(2-pyridylmethyl)amino]-p-cresol] (2,6-Htpcd). *Inorg Chem.* 2012 Jan 2;51(1):88–97.
22. Mergehenn R, Merz L, Haase W, Allmann R. Die Kristallstruktur des tetrameren Cu(II)-Komplexes mit 7-Hydroxy-4-methyl-5-azahept-4-en-2-on in  $\beta$ -(C<sub>7</sub>H<sub>11</sub>NO<sub>2</sub>Cu).2C<sub>6</sub>H<sub>6</sub>[ $\beta$ -(CuEIA)4.2C<sub>6</sub>H<sub>6</sub>]. *Acta Crystallogr B.* 1976 Feb 1;32(2):505–10.
23. Haase W. Exchange interactions in tetranuclear copper(II) complexes. *Journal of Molecular Catalysis.* 1984 Mar;23(2–3):331–40.
24. Mergehenn R, Merz L, Haase W. Crystal and molecular structure and magnetic properties of tetrakis-[bromo(2-diethylaminoethanolato)copper(II)]-tetrachloromethane (1/4), a complex with a ferromagnetic ground state. *J Chem Soc, Dalton Trans.* 1980;(9):1703–9.
25. Ruiz E, Rodríguez-Forte A, Alemany P, Alvarez S. Density functional study of the exchange coupling in distorted cubane complexes containing the Cu<sub>4</sub>O<sub>4</sub> core. *Polyhedron.* 2001 May;20(11–14):1323–7.
26. Burgos-Lopez Y, Del Plá J, Balsa LM, León IE, Echeverría GA, Piro OE, et al. Synthesis, crystal structure and cytotoxicity assays of a copper(II) nitrate complex with a tridentate ONO acylhydrazone ligand. Spectroscopic and theoretical studies of the complex and its ligand. *Inorganica Chim Acta.* 2019 Mar 1;487:31–40.
27. Burgos-López Y, Balsa LM, Piro OE, León IE, García-Tojal J, Echeverría GA, et al. Tridentate acylhydrazone copper(II) complexes with heterocyclic bases as coligands. Synthesis, spectroscopic studies, crystal structure and cytotoxicity assays. *Polyhedron.* 2022 Feb 1;213.
28. Rodríguez MR, Balsa LM, Piro OE, Echeverría GA, García-Tojal J, Pis-Diez R, et al. Synthesis, Crystal Structure, Spectroscopic Characterization, DFT Calculations and Cytotoxicity Assays of a New Cu(II) Complex with an Acylhydrazone Ligand Derived from Thiophene. *Inorganics (Basel).* 2021 Jan 20;9(2):9.
29. Santa María de la Parra L, Romo AIB, Rodríguez-López J, Nascimento OR, Echeverría GA, Piro OE, et al. Promising Dual Anticancer and Antimetastatic Action by a Cu(II)

- Complex Derived from Acylhydrazone on Human Osteosarcoma Models. *Inorg Chem.* 2024 Mar 18;
30. El-Gammal OA, El-Reash GMA, Bedier RA. Synthesis, spectroscopic, DFT, biological studies and molecular docking of oxovanadium (IV), copper (II) and iron (III) complexes of a new hydrazone derived from heterocyclic hydrazide. *Appl Organomet Chem.* 2019 Oct 13;33(10).
  31. Farrugia LJ. WinGX and ORTEP for Windows: An update. *J Appl Crystallogr.* 2012 Aug;45(4):849–54.
  32. Aliyeva VA, Gurbanov A V., Gomila RM, Frontera A, André V, Martins LMDRS, et al. Substituent Effect on Regium Bonding in Copper(II) Complexes of 4-Substituted Pyridines: Crystallographic and Computational Study. *Cryst Growth Des.* 2024 Oct 3;
  33. Lo Iacono C, Pizzi A, Mahmudov KT, Gomila RM, Frontera A, Resnati G. When CuCl<sub>4</sub><sup>2-</sup> and CuBr<sub>4</sub><sup>2-</sup> Form Anion...Anion Networks Assembled via Cu...Cl/Br Regium Bonds. *Cryst Growth Des.* 2025 Jun 18;25(12):4338–47.
  34. Bianchi R, Gervasio G, Marabello D. Experimental Electron Density Analysis of Mn(CO)<sub>10</sub>: Metal–Metal and Metal–Ligand Bond Characterization. *Inorg Chem.* 2000 May 1;39(11):2360–6.
  35. Goodenough JB. Theory of the Role of Covalence in the Perovskite-Type Manganites [La, M(II)]MnO<sub>3</sub>. *Physical Review.* 1955 Oct 15;100(2):564–73.
  36. Goodenough JB. An interpretation of the magnetic properties of the perovskite-type mixed crystals La<sub>1-x</sub>Sr<sub>x</sub>CoO<sub>3-λ</sub>. *Journal of Physics and Chemistry of Solids.* 1958 Aug;6(2–3):287–97.
  37. Kanamori J. Superexchange interaction and symmetry properties of electron orbitals. *Journal of Physics and Chemistry of Solids.* 1959 Jul;10(2–3):87–98.
  38. Anderson PW. Antiferromagnetism. Theory of Superexchange Interaction. *Physical Review.* 1950 Jul 15;79(2):350–6.
  39. De L D Landau EML. Identity of Particles. In: *Quantum Mechanics: Non-Relativistic Theory.* 3rd ed. Oxford: Pergamon Press; 1977.
  40. Chandrasekhar V, Senapati T, Dey A, Sañudo EC. Rational Assembly of Soluble Copper(II) Phosphonates: Synthesis, Structure and Magnetism of Molecular Tetranuclear Copper(II) Phosphonates. *Inorg Chem.* 2011 Feb 21;50(4):1420–8.
  41. Bencini A, Gatteschi D, Zanchini C, Haasnoot JG, Prins R, Reedijk J. On the nature of the low-lying electronic levels of a tetranuclear copper(II) complex. *J Am Chem Soc.* 1987 May 1;109(10):2926–31. DOI: 10.1039/D5DT01463H
  42. van Koningsbruggen PJ, Müller E, Haasnoot JG, Reedijk J. A novel tetranuclear copper(II) cluster containing twisted hydrazide bridges. X-ray crystal structure and magnetic properties of tetrakis[N,N'-imidopicolinyloxamylhydrazine]copper(II) tetranitrate octahydrate. *Inorganica Chim Acta.* 1993 Jun;208(1):37–42.
  43. Tercero J, Ruiz E, Alvarez S, Rodríguez-Forteza A, Alemany P. Density functional study of magnetostructural correlations in cubane complexes containing the Cu<sub>4</sub>O<sub>4</sub> core. *J Mater Chem.* 2006;16(26):2729–35.
  44. Chilton NF, Anderson RP, Turner LD, Soncini A, Murray KS. PHI: A powerful new program for the analysis of anisotropic monomeric and exchange-coupled polynuclear d- and f-block complexes. *J Comput Chem.* 2013 May 15;34(13):1164–75.
  45. Bencini A, Gatteschi D. *Electron Paramagnetic Resonance of Exchange Coupled Systems.* Berlin, Heidelberg: Springer Berlin Heidelberg; 1990.
  46. Hathaway BJ, Billing DE. The electronic properties and stereochemistry of mono-nuclear complexes of the copper(II) ion. *Coord Chem Rev.* 1970 Jul;5(2):143–207.
  47. Rocha M, Ruiz MC, Echeverría GA, Piro OE, Di Virgilio AL, León IE, et al. Diethylaminophenyl-based Schiff base Cu(II) and V(IV) complexes: experimental and theoretical studies and cytotoxicity assays. *New Journal of Chemistry.* 2019;43(47):18832–42.
  48. Hathaway BJ. The correlation of the electronic properties and stereochemistry of mononuclear {CuN<sub>4</sub>–6} chromophores. *J Chem Soc, Dalton Trans.* 1972;(12):1196–9.
  49. Rigaku. CrysAlisPro 1.171.38.41. Oxford Diffraction, UK. 2015;
  50. Sheldrick GM. SHELXT– Integrated space-group and crystal-structure determination. *Acta Crystallogr A Found Adv.* 2015 Jan 1;71(1):3–8.
  51. Sheldrick GM. A short history of SHELX. *Acta Crystallogr A.* 2008 Jan 1;64(1):112–22.
  52. McKinnon JJ, Spackman MA, Mitchell AS. Novel tools for visualizing and exploring intermolecular interactions in molecular crystals. *Acta Crystallogr B.* 2004 Dec 1;60(6):627–68.

## ARTICLE

## Journal Name

53. Luo YH, Chen C, Hong DL, He XT, Wang JW, Sun BW. Thermal-Induced Dielectric Switching with 40K Wide Hysteresis Loop Near Room Temperature. *J Phys Chem Lett.* 2018 May 3;9(9):2158–63.
54. McKinnon JJ, Jayatilaka D, Spackman MA. Towards quantitative analysis of intermolecular interactions with Hirshfeld surfaces. *Chemical Communications.* 2007;(37):3814–6.
55. Spackman MA, Jayatilaka D. Hirshfeld surface analysis. *CrystEngComm.* 2009;11(1):19–32.
56. Spackman MA. Molecular electric moments from x-ray diffraction data. *Chem Rev.* 1992 Dec 1;92(8):1769–97.
57. Spackman PR, Turner MJ, McKinnon JJ, Wolff SK, Grimwood DJ, Jayatilaka D, et al. CrystalExplorer: a program for Hirshfeld surface analysis, visualization and quantitative analysis of molecular crystals. *J Appl Crystallogr.* 2021 Jun 1;54(3):1006–11.
58. Adamo C, Barone V. Toward reliable density functional methods without adjustable parameters: The PBE0 model. *J Chem Phys.* 1999 Apr 1;110(13):6158–70.
59. Caldeweyher E, Bannwarth C, Grimme S. Extension of the D3 dispersion coefficient model. *J Chem Phys.* 2017 Jul 21;147(3).
60. Weigend F. Accurate Coulomb-fitting basis sets for H to Rn. *Physical Chemistry Chemical Physics.* 2006;8(9):1057–65.
61. M. J. Frisch, G. W. Trucks, H. B. Schlegel, G. E. Scuseria .., J. B. Foresman, D. J. Fox. Gaussian 16 Revision C. 01, 2016. Gaussian Inc Wallingford CT. 2016;1:572.
62. Bader RFW. A quantum theory of molecular structure and its applications. *Chem Rev.* 1991 Jul 1;91(5):893–928.
63. Lu T, Chen F. Multiwfn: A multifunctional wavefunction analyzer. *J Comput Chem.* 2012 Feb 15;33(5):580–92.
64. Contreras-García J, Johnson ER, Keinan S, Chaudret R, Piquemal JP, Beratan DN, et al. NCIPLOT: A Program for Plotting Noncovalent Interaction Regions. *J Chem Theory Comput.* 2011 Mar 8;7(3):625–32.
65. Becke AD, Edgecombe KE. A simple measure of electron localization in atomic and molecular systems. *J Chem Phys.* 1990 May 1;92(9):5397–403.
66. Humphrey W, Dalke A, Schulten K. VMD: Visual molecular dynamics. *J Mol Graph.* 1996 Feb;14(1):33–8.

View Article Online  
DOI: 10.1039/D5DT01463H

The data supporting this article have been included as part of the Supplementary Information: [View Article Online](#)  
DOI: 10.1039/D5DT01463H

X-ray crystallographic data. Tables of crystal data for H<sub>2</sub>L ligand and its Cu<sub>4</sub>L<sub>4</sub> complex (Table X1), bond distances of H<sub>2</sub>L and charged L<sub>2</sub><sup>-</sup> ligand in Cu<sub>4</sub>L<sub>4</sub> complex (Table X2), bond lengths and angles around copper in Cu<sub>4</sub>L<sub>4</sub> complex (Table X3), fractional coordinates and equivalent isotropic displacement parameters of the non-H atoms of H<sub>2</sub>L ligand and the Cu<sub>4</sub>L<sub>4</sub> complex (Tables X4a,b), full bond distances and angles (Tables X5a,b), atomic anisotropic displacement parameters (Tables X6a,b), hydrogen atoms positions (Tables X7a,b), torsion bond angles (Tables X8a,b), and H-bond distances and angles (Table X9a), assignment of the most significant vibrational modes for H<sub>2</sub>L and Cu<sub>4</sub>L<sub>4</sub> (Table X10). Crystallographic structural data have been deposited at the Cambridge Crystallographic Data Centre (CCDC). Any request to the Cambridge Crystallographic Data Centre for this material should quote the full literature citation and the reference number CCDC 2260992 (H<sub>2</sub>L) and 2260081 (Cu<sub>4</sub>L<sub>4</sub>).

Magnetic properties. Unpaired electrons spin levels and analytical expression for magnetic susceptibility (Sect. M1); Magnetic susceptibility (Sect. M2); Curie-Weiss behaviour (Sect. M3); Powder EPR spectra (Sect. M4), and Single crystal EPR spectra (Sect. M5).

•